Advances in Colloid and Interface Science 206 (2014) 250–264

Contents lists available at ScienceDirect

Advances in Colloid and Interface Science

journal homepage: www.elsevier.com/locate/cis

Evaporation-driven instability of the precorneal tear film

Cheng-Chun Peng [a], Colin Cerretani [a], Richard J. Braun [b], C.J. Radke [a,c,*]

[a] Department of Chemical and Biomolecular Engineering, University of California, Berkeley, CA, 94720, United States
[b] Department of Mathematical Sciences, University of Delaware, Newark, DE, 19716, United States
[c] Vision Science Group, University of California, Berkeley, CA, 94720, United States

ARTICLE INFO

Available online 6 June 2013

Keywords:
Tear-film stability
Evaporation
Dry eye
Hyperosmolarity
Tear-film lipid layer

ABSTRACT

Tear-film instability is widely believed to be a signature of eye health. When an interblink is prolonged, randomly distributed ruptures occur in the tear film. "Black spots" and/or "black streaks" appear in 15 to 40 s for normal individuals. For people who suffer from dry eye, tear-film breakup time (BUT) is typically less than a few seconds. To date, however, there is no satisfactory quantitative explanation for the origin of tear rupture.

Recently, it was proposed that tear-film breakup is related to locally high evaporative thinning. A spatial variation in the thickness of the tear-film lipid layer (TFLL) may lead to locally elevated evaporation and subsequent tear-film breakup. We examine the local-evaporation-driven tear-film-rupture hypothesis in a one-dimensional (1-D) model for the evolution of a thin aqueous tear film overriding the cornea subject to locally elevated evaporation at its anterior surface and osmotic water influx at its posterior surface. Evaporation rate depends on mass transfer both through the coating lipid layer and through ambient air. We establish that evaporation-driven tear-film breakup can occur under normal conditions but only for higher aqueous evaporation rates. Predicted roles of environmental conditions, such as wind speed and relative humidity, on tear-film stability agree with clinical observations. More importantly, locally elevated evaporation leads to hyperosmolar spots in the tear film and, hence, vulnerability to epithelial irritation. In addition to evaporation rate, tear-film instability depends on the strength of healing flow from the neighboring region outside the breakup region, which is determined by the surface tension at the tear-film surface and by the repulsive thin-film disjoining pressure. This study provides a physically consistent and quantitative explanation for the formation of black streaks and spots in the human tear film during an interblink.

Contents

* Corresponding author at: Chemical and Biomolecular Engineering Department, University of California, 101E Gilman, Berkeley, CA94720-1462, United States. Tel.: +1 510 642 5204; fax: +1 510 642 4778.
E-mail address: radke@berkeley.edu (C.J. Radke).

0001-8686/$ – see front matter
http://dx.doi.org/10.1016/j.cis.2013.06.001

1. Introduction

The phenomenon of tear-film breakup was observed in the 1960s when aqueous sodium fluorescein was applied for ophthalmic clinical evaluation [1–3]. When blinking is slowed, randomly distributed "black spots" and/or "black streaks" develop in the tear film in 15 to 40 s [4,5]. For subjects who suffer from dry eye, ruptures can appear in a few seconds [6]. Thus, measurement of tear-film stability by fluorescein breakup time (FBUT), i.e., the elapsed time between the end of a complete blink and the first appearance of randomly distributed black spots [4], has been widely used as a diagnostic aid to ascertain dry-eye syndromes [7].

Tear rupture is easily seen in slit-lamp examination as rapidly expanding dark circular spots, linear streaks, or irregular pools on a yellow-green fluorescence background [8]. The tear film in humans is generally described as a three-layer film [9]. The aqueous layer, where the applied fluorescein marker participates, is the main component. The average thickness of the aqueous layer was thought be 7 μm when the three-layer model was proposed [9]. Recent studies, however, suggest that the average aqueous tear thickness is around 3 μm [10]. A thin (~0.1 μm) tear-film lipid layer (TFLL) covers the bulk aqueous layer [9], and a spatially feathered mucous-rich region (~0.2–0.5 μm) resides in the aqueous layer directly adjacent to the corneal epithelium [11–16]. Each region of the tear plays specific roles in the maintenance of health and normal function of the eye [17].

Black spots/streaks observed under fluorometry are typically interpreted as local holes where the aqueous layer of the tear film completely ruptures down to the underlying mucin/corneal interface, exposing the epithelium to air [18]. The mechanism(s) of tear-film breakup remain clouded in spite of several decades of attention. We first review previous models of tear-film rupture and their underlying physical mechanisms in Section 2. Subsequently in Section 3, we outline the physics of the newly proposed evaporation-driven tear-film breakup model. Results of the numerical modeling work based on this evaporation-driven tear-film breakup model are reported and discussed in Section 4. Sections 5 and 6 present discussion of the model assumptions and conclusions, respectively.

2. Tear-film breakup mechanism(s)

The first proposed tear-film breakup mechanism by Holly [18] attributed rapid tear-film breakup to migration of lipids from the TFLL towards the mucous region and adsorption of these lipids to the glycocalyx membrane-bound mucin. Lipid adsorption was thought to expose the polar end of the lipid molecule to the aqueous tear film, which then breaks locally over the lipid-contaminated region due to increased epithelium hydrophobicity. Unfortunately, numerous physical flaws exist in this proposed mechanism [19–23], including lack of a driving force for lipid adsorption, inconsistency between the time scale of lipid molecular diffusion and film rupture, lipid equilibration in the aqueous tear, soluble mucin redistribution over long time, failure to explain localized rupture, and breakup in subjects with lipid deficiency.

In the early 1980s, researchers studied tear-film breakup using hydrodynamic stability analyses of thin liquid films on a solid substrate under the hypothesized influence of van der Waals dispersion forces [20–25]. Two primary competing forces affected tear-film stability. The first is capillarity or curvature-driven flow that heals local disturbances within the tear film and enhances stability. The healing effect of capillarity is responsible for maintaining a smooth refractive tear surface for clear vision. The second is flow driven by thin-film forces, known commonly as Hamaker forces [26,27] that are expressed as an excess pressure within the film, Π, the conjoining/disjoining pressure. If the epithelium subsurface supporting tear film is hydrophobic, the Hamaker force is purely attractive (conjoining) and varies with film thickness, h, as $-A/6\pi h^3$ [26,27], where A is the Hamaker constant characteristic of the substrate and liquid phases. For very thin films, attractive Hamaker forces (i.e., $A > 0$) can overpower the stabilizing curvature forces leading to film rupture. Lin and Brenner [22] first conducted a linear stability analysis of a thin-film model for human tear film and concluded that an attractive Hamaker dispersion force can initiate tear-film rupture. However, the accepted magnitude range for A lies between 10^{-19} and 10^{-21} J [26,27]. Accordingly, the film thickness that is vulnerable to rupture in a reasonable time frame, even upon invoking hydrodynamic slip at the epithelium surface, must be less than about 100 nm [28,29]. This value is two orders of magnitude smaller than the accepted overall thickness of the tear film. Thus, although attractive Hamaker forces are well-accepted for hydrophobic solid surfaces [26], they are unlikely the origin of rupture in the human tear film.

In a second early contribution [23], Lin and Brenner considered the role of Marangoni flow (i.e., surface-tension-gradient-driven tangential flow) in tear-film rupture. They, and others following [20,21,24,25,29–37], treat the TFLL as a classical submonolayer surfactant adsorbed at the air/water interface with a spatial variation of surface tension that induces tear flow. In a region of local instability thinning, surfactant adsorption is smaller than that of the surrounding tear film. Hence, the corresponding local surface tension is higher than that of the surrounding tear, and flow is directed toward the region of higher tension to heal the growing instability. Thus, classical Marangoni flow retards tear-film rupture [20,21,23–25,29–37].

Immediately following a blink, the TFLL spreads upwards [31,38–40] most likely due to thickness-dependent conjoining/disjoining forces in the lipid layer or equivalently to a thin-film tension gradient arising from thickness variation of the lipid layer [41]. However, net upward flow of the TFLL stops in about 1–2 s and does not contribute to pre-corneal tear-film instability during the subsequent portion of the interblink. Once the TFLL stabilizes, interfacial flows apparently do not induce typical tear-film rupture [38,42].

In 1985, Sharma and Ruckenstein emphasized the insufficiency of classical Hamaker forces for destabilizing the human tear film and proposed an alternative explanation [20,21]. They envisioned a distinct soluble-mucous layer residing next to a hydrophobic cornea and over-ridden by a thick aqueous tear film. The mucin layer was thin and subject to attractive Hamaker dispersion forces (~100 nm). In a two-step process, conjoining Hamaker forces break the thin soluble-mucin sublayer and expose the aqueous tear film to a hydrophobic epithelium. Rupture of the mucous layer in turn, is stated, but not proved, to rupture the thick overlying tear film (i.e., of initial thickness beyond the range of thin-film forces).

Subsequently, Sharma and Ruckenstein extended the distinct mucous-layer model to account for the lipid layer [24,25]. In their second model, lipid exhibits finite solubility in the aqueous and mucous phases and behaves as an "antisurfactant" (i.e., undergoes net desorption) at the mucous/aqueous interface raising the interfacial tension there and stabilizing the mucous layer through Marangoni flow. Although their extended two-step model correlates several clinical observations of human tear-film breakup, including lipid abnormalities, and aqueous and mucus deficiencies, it is arguable that human lipid is aqueous soluble.

More importantly, subsequent breakup of the thick tear film following rupture of the mucous layer remained unquantified.

More recently, Zhang et al. amplified the distinct mucin-layer model to include non-Newtonian rheology of aqueous mucus and to treat the lipid layer as an insoluble surfactant submonolayer at the air/water interface [32,33]. These authors explicitly include the overriding thick tear film in their stability formulation and show that the mucous-layer instability of Sharma and Ruckenstein thins the bounding thick tear film. Unfortunately, calculations were not carried beyond the rupture time of the mucous layer where the locally thinned tear layer remains of finite thickness. It is not established whether the bounding tear film eventually ruptures or whether the necessary additional time for tear breakup (BUT) after mucin rupture is reasonable.

The view that there is a distinct, well-defined soluble-mucous layer appears incorrect in most recent findings [11–13]. No sharp interface exists between the aqueous and mucous regions in human tear [10,14–16,43]. Even if the mucous region is approximated as a distinct layer coating a hydrophobic surface, rupture within clinically observed time frames (BUT) in these models demands an extremely thin soluble-mucin layer of 20–40 nm [20–25,29,32,33]. Critically, the membrane-bound mucin molecules protruding from the anterior epithelium (i.e., the glycocalyx) are highly water-liking [11–13]. This fact, plus the folded microplicae structure of the corneal anterior surface [44] argue strongly against a hydrophobic corneal surface.

It is now generally accepted that a healthy corneal epithelium exhibits a water-wet surface [45–47]. Thus, it is thermodynamically unfavorable to eliminate mucin/cornea and mucin/aqueous interfaces in favor of a single cornea/aqueous interface [28]. For a water-wet corneal surface, Hamaker dispersion forces are repulsive, i.e., the Hamaker constant is negative, and no dewetting of the tear film is possible. Thus, the physical basis for the distinct mucous-layer model of tear rupture must be questioned. In spite of statements to the contrary [32], no experimental evidence exists confirming that a thin unstable fluid layer sandwiched between a solid and a thick bounding film can destabilize the thicker film within clinically relevant breakup times [48–50]. Although numerous factors, including Marangoni stress, hydrodynamic slip, surface diffusion of adsorbed surfactants, gravity, capillarity, lipid solubility, thin-film forces, and rheology are discussed in earlier works [51], no physically viable mechanism is yet available to explain human tear-film rupture.

Early on, tear-film evaporation instability was ruled out based on the observation that the overall thickness of the tear film (~7 μm) decreases by only about 10% due to evaporation during a 15–40 s interblink under normal conditions (~0.75 μm/min) [52–54]. Recent studies, however, suggest that the average aqueous tear thickness is thinner (~3 μm) [10], and that the normal evaporation rate of pre-corneal tear-film in "free-air" conditions may be four to five times faster than that measured in goggles [55–58].

Here, we re-visit the possibility of evaporation-driven tear-film breakup [56,59]. The underlying picture is that the TFLL covering aqueous tear is very thin and not necessarily stable [59–63]. Any breakup spots in the lipid layer expose the water/lipid interface directly to air. Since the TFLL acts as a barrier to water evaporation from the underlying tear [53], local lipid-layer rupture leads to high evaporation rates that potentially drive rupture of the tear film [64].

As in the Hamaker-driven instability, a growing evaporation hole is opposed by curvature-driven flow that attempts to fill in that hole. Thus, only if the water evaporation rate is sufficient to overcome capillary healing flow does rupture occur. In addition, curvature-driven opposition flow brings in salt from the surrounding thicker tear film. Salt concentration then builds directly underneath the deepening hole as salt molecular diffusion is typically slow compared to convection. Further, water locally evaporates further concentrating the salt just below the rupture hole. Such local salinity "hot spots" in the tear film have been suggested [65] but not verified. Locally high salt content underneath a growing hole increases the osmolarity there and draws water locally from the cornea. Osmotic-driven flow is a second means to heal a deepening dimple. To rupture the tear film, evaporation rates must be large enough to overcome both curvature-driven and osmotic-driven healing water flow. Only a quantitative analysis of the proposed evaporation-driven instability can assess the reasonableness of the hypothesis.

We examine quantitatively evaporation-driven tear-film breakup in a 1-D mathematical model including simultaneous evolution of and osmolarity distribution within a solid-supported thick (~3.5 μm) aqueous tear film subject to evaporation at its anterior surface and osmotic water influx at its posterior surface. The localized tear-film instability is initiated by breakup of the TFLL, leading to localized elevated evaporation. Inclusion of both evaporation and osmotic effects in a dynamic tear-film-thinning model is requisite to represent environmental effects on tear-film stability, such as relative humidity and air flow. To determine the feasibility of evaporation-driven tear-film rupture, model predictions are compared with current clinical observations.

3. Physics of evaporation-driven tear-film breakup

3.1. Tear-film dynamics

We outline a 1-D model for the evolution of a thin aqueous tear film bounding the cornea based on a two-layer tear-film model [11–13]. A single Newtonian fluid layer represents the aqueous layer of the tear film including distributed soluble mucin with a thin overriding lipid layer. No distinctive mucous region is explicitly defined in our model. Adoption of Cartesian coordinates specifies a "black streak" whereas cylindrical coordinates give rise to a "black spot". In our analysis, initial rupture events are considered independent. Fig. 1 illustrates that both black spots and streaks are common. Fig. 2 is a schematic of the rupture process, defining the relevant dimensions, fluxes, water and salt concentrations, and temperatures.

The tear film is "perched" by the black lines formed immediately after tear-film deposition due to capillary suction from the menisci at the lid margins [66,67]. As illustrated in Fig. 2, the local position in the tear film along the palpebral aperture of length 2 L is denoted by x, where $x = 0$ represents the center of the corneal surface, and $x = \pm L$ indicates the upper and lower black lines near the lid margins. The curvature of the cornea under the tear film is neglected since the thickness of the tear film is three orders of magnitude smaller than the diameter of the pre-corneal tear film [51,68]. The z-coordinate denotes the direction normal to the corneal/conjunctival surface, where $z = 0$ and $z = h$ represent the tear/cornea and tear/air (or tear/lipid) interfaces, respectively. The posterior corneal/tear interface ($z = 0$), is considered a semipermeable membrane that allows

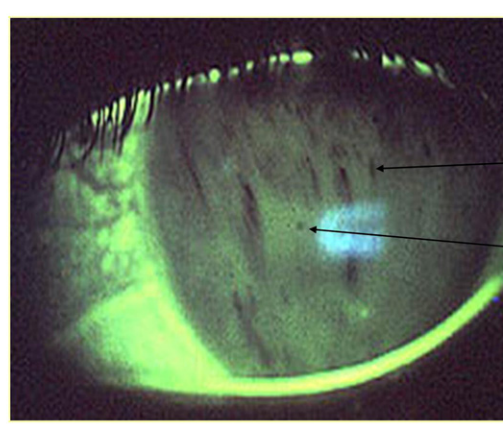

Fig. 1. Typical tear-film breakup image under fluorescence slit-lamp examination. Dark regions with various shapes appear against the yellow-green background indicate the tear-film breakup. Photo courtesy of J. L. Creech [19].

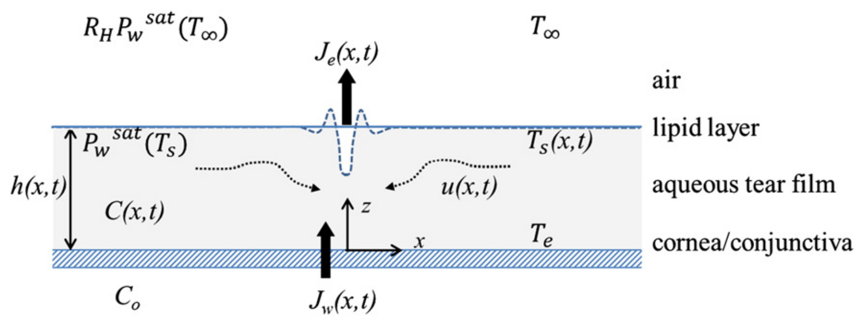

Fig. 2. Schematic of the precorneal tear film with salt concentrations (C), temperatures (T), and fluxes (J) labeled. J_w is the osmotic water flux that depends on the local salt concentration. J_e is the evaporation flux that depends on both the thickness of TFLL and the vapor pressure difference between the tear/air interface and the environment. T_e is the constant corneal temperature, and T_S is the tear/lipid interface temperature of corresponding vapor pressure $P_W^{sat}(T_S)$. The dashed line illustrates a growing tear-film instability. Drawing is not to scale.

weeping flow generated in response to tear osmolarity [51,69,70]. The tear/air interface is located at $z = h$, where water is lost through evaporation across the entire film. A thick solid line at the outer edge of the tear film demarks an intact lipid layer. The dashed portion of this line indicates a region of lipid breakup and corresponding larger water evaporation rate in the region of TFLL rupture. An increased evaporation rate relative to that of the surrounding film initiates a growing dimple in the tear. The resulting curved water interface draws tear into the dimple to heal the growing hole, as shown by curved dotted lines in the film labeled by the flow velocity, u. Underneath the growing hole at thickness $h(0,t)$, the local salt concentration, $C(0,t)$, is elevated compared to that in the bulk of the tear film. An elevated salt concentration osmotically draws more water through the cornea compared to that into the encompassing lower-salt concentration tear film. Tear breakup occurs only when the evaporation rate in the growing dimple (or trough) exceeds the curvature- and osmotic-driven healing flows.

3.2. Breakup model

To assess the feasibility of evaporation-driven black spots/streaks in a human tear film, we write continuum mass, momentum, and energy conservation balances for water and salt. Tear-film dynamics in this model are similar to those of Braun et al. [64] and Winter et al. [71], but with important differences in the underlying physics for the evaporation rate. In the current study, the evaporation rate depends on mass-transfer rates rather than on molecular kinetics. Hence, the evaporative flux of water depends inversely on the sum of a gas-phase mass-transfer resistance, R_G, and a TFLL mass-transfer resistance, R_F, and directly on the difference between the tear-film surface vapor pressure and the environment water partial pressure. Details are available in Appendix A. In this section, we briefly summarize the proposed tear-film dynamics model. Since the tear film is much thinner than its lateral extent, the lubrication approximation is pertinent [72,73]. Conservation of water in the tear film reads

$$\frac{\partial h}{\partial t} = -J_e + J_w - \frac{\partial (uh)}{\partial x} \tag{1}$$

where $h(x,t)$ is the thickness of the film as a function of lateral distance and time, u is the z-averaged velocity in the x-direction, J_e is the evaporative volumetric flux of liquid water from the film into the environment (i.e., the mass flux divided by water mass density), and J_w is the weeping volumetric flux of water from the corneal epithelium into the tear film due to salt-induced osmosis (see Fig. 2). Rectangular coordinates in Eq. (1) reflect a single growing trough or black streak. Equations in radial coordinates that give rise to isolated black spots are outlined in Appendix A.

Eq. (1) contains the essence of an evaporative-driven tear instability. The three terms on the right correspond, respectively, to evaporative loss of film thickness, osmotic-healing flow of water into the deepening trough driven by locally high salt concentration, and healing flow into the trough due to curvature of the liquid/gas interface. Only when the right side of Eq. (1) is net negative can film rupture occur. This requires that J_e exceeds the magnitude of two healing flows. Far away from the growing canyon in Fig. 2, the TFLL is intact, and film thickness is uniform. Thus, the third term on the right of Eq. (1) vanishes. Nevertheless, evaporative loss through the intact TFLL overcomes osmotic weeping flow leading to an overall slow uniform decline in film thickness far from the trough instability. Over and above the general evaporative-film-thickness decline in the growing dimple is the enhanced evaporation rate in the lipid-deficient region that drives film rupture (see dashed line in Fig. 2).

Evaluation of Eq. (1) requires information on the evaporative flux J_e, the osmotic weeping flux, J_w, and the curvature-induced tangential volumetric flux u. These expressions are outlined in Appendix A. Clearly, however, the evaporative flux is the most important term, which is based on a relative-humidity driving force and impeded by a gas-phase mass-transfer resistance, R_G, and a TFLL diffusion resistance, R_F [60]

$$J_e = \frac{1}{\tilde{\rho}_w (R_F + R_G)} \left\{ \frac{P_w^{sat}(T_S)}{R_g T_S} \exp\left(-\frac{\gamma \frac{\partial^2 h}{\partial x^2} + \Pi(h)}{\tilde{\rho}_w R_g T_S} \right) - R_H \frac{P_w^{sat}(T_\infty)}{R_g T_\infty} \right\} \tag{2}$$

where $\tilde{\rho}_w$ is the molar density of liquid water, R_g is the ideal gas constant, $P_W^{sat}(T)$ is the saturation vapor pressure of water at temperature T, R_H is the ambient relative humidity, $T_S(x,t)$ is the local temperature of the liquid/air interface, and T_∞ is ambient temperature. The exponential factor in the first term of the parentheses corrects the vapor pressure at the water surface for curvature (i.e., surface tension, γ) and for thin-film conjoining/disjoining forces, $\Pi(h)$. This factor is established through a thermodynamic analysis analogous to that of Kelvin [26,74] and is detailed in Appendix A. An evaporation-driven instability gives rise to interface shapes analogous to that for a vapor bubble immersed in a liquid and pressed against a wall. The curved interface raises the local vapor pressure compared to that for a flat liquid/gas interface. Likewise, repulsive thin-film forces (i.e., positive Π) reduce the interface vapor pressure. The Kelvin correction in Eq. (2) disappears when there is no interface curvature or thin-film force. The effect of curvature on evaporation rate is always included in our calculations, whereas the effect of conjoining/disjoining pressure (Π) on the local vapor pressure of water is normally neglected. The exception is in Section 4.9.

In the air environment, the smaller the relative humidity, the faster is tear evaporation. Water evaporation encounters two resistances in series: that through the TFLL and that through the air phase

$$R_F + R_G = L_L(x)/D_w K_w + 1/k_m \tag{3}$$

where L_L is the local TFLL thickness, $D_w K_w$ is the permeability of water (i.e., the product of water diffusivity, D_w, and the partition coefficient, K_w) in the lipid film, and k_m is the mass-transfer coefficient of water in the air phase [60]. We set the lipid-rupture-thickness profile $L_L(x)$ to establish the local water evaporation rate. This procedure does not self-consistently capture the details of TFLL rupture but is consistent with experimental observation [59–64]. The highest water evaporation rate is that through a bare water/air interface where $L_L = 0$. Eqs. (2) and (3) describe the dependence of tear-film evaporation rate on both ocular and environmental factors [75]. Environmental factors include temperature, relative humidity, and flow velocity of the ambient air (i.e., via k_m); ocular factors include surface temperature, surface tension and conjoining/disjoining forces of the tear film, and the thickness of and water permeability in the TFLL.

Fig. 3 graphs the chosen lipid-layer thickness variation $L_L(x)$ by a solid line obeying a Gaussian distribution. With a standard deviation (S.D.) of 100 μm, a 0.2-mm wide break in the lipid layer exists where the lipid layer ruptures from a thickness of 100 nm down to zero thickness corresponding to a bare water/air interface. Water evaporates more quickly in the lipid-deficient rupture canyon following Eqs. (2) and (3), as shown by the dashed line in Fig. 3. For the conditions chosen in Fig. 3, the bare water interface evaporates at 38 μm/min estimated for an average perpendicular-impinging wind speed of 0.3 m/s characteristic of indoor workplaces [76]. Far away from the lipid rupture, a fully intact lipid layer reduces the evaporation rate of water by 90% to 3.8 μm/min, which is an average tear-film evaporation rate measured clinically [56]. Many other lipid-rupture sizes, lipid thicknesses, and corresponding water evaporation rates can be investigated by changing the appropriate parameters in Eqs. (2) and (3).

Due to evaporative cooling, the temperature of the water/air interface, $T_S(x,t)$, is lower than that of the eye, and is unknown in Eq. (2). Energy conservation determines this temperature

$$\frac{J_e \Delta \hat{H}_v}{\rho_w} = k_w \left(\frac{T_e - T_S(x,t)}{h(x,t)} \right) + U[T_\infty - T_S(x,t)] \tag{4}$$

where ρ_w is the mass density of liquid water, $\Delta \hat{H}_v$ is the specific enthalpy of water vaporization, k_w is the thermal conductivity of aqueous tear, T_e is eye temperature (35 °C), T_∞ is the temperature of the surroundings, and U is the gas-phase heat transfer coefficient, i.e., $1/U$ is the resistance to heat transfer in the environment. Energy is required to evaporate water. Eq. (4) specifies that heat conducted from the warm eye at T_e and convected towards the environment at T_∞ sets the local temperature of the tear/air surface, $T_S(x,t)$. The two terms on the right of Eq. (4) quantify these two respective processes.

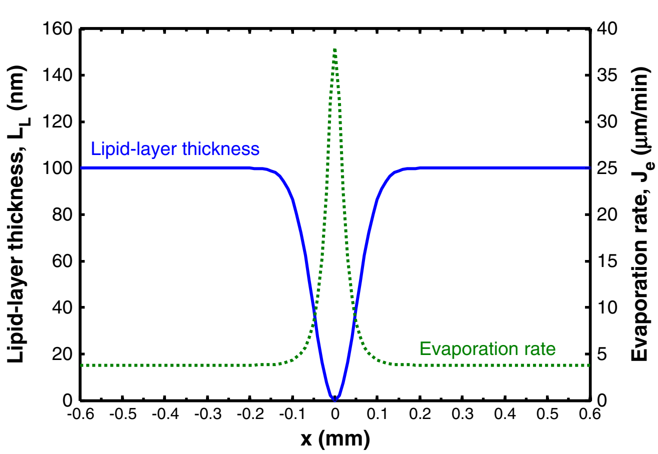

Fig. 3. Dependence of evaporation rate on TFLL thickness. The chosen lipid-layer thickness variation $L_L(x)$ is shown by a solid line obeying a Gaussian distribution with a standard deviation (S.D.) of 100 μm. The corresponding volumetric evaporation rate, J_e, (dashed line), from a 3.5-μm thick tear film is determined from Eqs. (2) and (3) with parameters given in Table 1.

Table 1
Physical properties.

Parameter	Description	Value	Unit	Ref
C_o	Initial osmolarity in tear film	300	mOsM	[69]
D	Salt diffusivity in the tear film	1.5×10^{-9}	m^2/s	[93]
D_wK_w	Water permeability in lipid-layer	2.2×10^{-10}	m^2/s	Appendix A
h_o	Initial thickness of tear film	3.5	μm	[10]
k_w	Thermal conductivity of tear film	0.60	W/m·K	[92]
M_w	Molecular weight of water	0.018	kg/mol	
P_c	Corneal water permeability	2.3×10^{-10}	m/s/mOsM	[64]
$P_w^{sat}(T_\infty)$	Water vapor pressure at T_∞	3143.7	Pa	[94]
R_g	Ideal gas constant	8.31	J/mol·K	
$R_G = 1/k_m$	Mass-transfer resistance in ambient air	51.55	s/m	Appendix A
R_H	Relative humidity	0.3	[−]	
T_∞	Ambient air temperature	25	°C	
T_e	Temperature at the surface of cornea	35	°C	
U	Heat exchange coefficient of air	20.7	$W/m^2 \cdot K$	Appendix A
γ	Surface tension of tear film	4.5×10^{-2}	N/m	[67,95]
$\Delta \hat{H}_v$	Specific latent heat of evaporation	2.43×10^6	J/kg	[94]
ρ_w	Mass density of water	1000	kg/m^3	

Osmotic weeping flow, J_w in Eq. (1), is proportional to the difference between the concentration of salt in the aqueous tear and that in the anterior chamber, $J_w(x,t) = P_c(C(x,t) - C_0)$ where $C(x,t)$ is the z-averaged salt concentration in the tear film expressed in osmolarity units, C_0 is the serum salt concentration (300 mOsM), and P_c is the corneal salt permeability [69,70]. The local tear salt concentration must be known to determine J_w. Conservation of salt in the perched tear film demands that

$$h\frac{\partial C}{\partial t} = C(J_e - J_w) + D\frac{\partial}{\partial x}\left(h\frac{\partial C}{\partial x}\right) - uh\frac{\partial C}{\partial x} \tag{5}$$

where D is the diffusion coefficient of aqueous sodium chloride. Since the water evaporative flux is larger than the weeping flux, the first term on the right of Eq. (5) increases the salt concentration in the tear. The local increase in salt concentration underneath the growing instability, where the evaporation rate is the highest, is partially mitigated by diffusion of salt out from underneath the trough, as described by the second term on the right of Eq. (5). Diffusive transport of salt away from the instability trough is offset by fluid convection into that region, as quantified by the third term on the right of Eq. (5). Since uh/D is much greater than unity (i.e., diffusion is slow compared to convection) the increased salt concentration arising from locally high evaporation is augmented by salt inflow from surrounding tear. Essentially, salt is trapped underneath a growing tear instability leading to a local "hot spot" in salt concentration. This same argument holds for any nonvolatile aqueous solute including proteins, soluble mucins, and dyes.

Finally, the volumetric flux, u in Eqs. (1) and (5), is obtained from curvature-driven tangential flow according to Laplace's law of surface tension as described in Appendix A. Thin-film or Hamaker forces can also influence tear flow, but in our case, only extremely near the corneal epithelium in the region of the glycocalyx. Thus, in some illustrative calculations, we include a repulsive (disjoining) thin-film excess pressure. A thin-film disjoining force prevents the glycogalyx from drying out immediately adjacent to the corneal epithelium thereby maintaining a water-wet cornea even in a ruptured tear film [51,71]. Model details and calculation procedures are discussed in Appendix A and below. Because initial TFLL breakup is not addressed, our analysis gauges the feasibility of evaporative-driven tear-film rupture.

4. Results and discussion

4.1. Rupture dynamics

Fig. 4A portrays a tear-rupture streak initiated by the imposed precursor TFLL break and resulting local elevated evaporation rate in Fig. 3. Except in Section 4.9, thin-film forces are not accounted for (i.e., $\Pi = 0$). The ordinate and abscissa scales in this figure, and in those to follow, are quite different. In reality, the rupture streak in Fig. 4A is thin and flat compared to its depth, consonant with a lubrication analysis. After 5 s in Fig. 4A, a noticeable depression is evident that is wider than the TFLL rupture. This depression narrows and deepens quickly until complete tear rupture occurs at about 33 s. If observed under fluorescein instillation, the trough becomes black when the tear film underneath it nears zero thickness. Outside the rupture trough, tear-film thickness declines uniformly and more slowly because of the protection afforded by the intact TFLL against tear evaporation. A small narrow rim forms just beyond the growing instability. The curvature along the deepening canyon wall drives infill flow from surrounding tear. However, the large flow resistance in the very thin film underneath the trough prevents much healing. The result is a thickening rim just outside the instability as tear accumulates there. Fig. 4B compares the film thickness at the center, h_T, and far from the center of the rupture streak, h_F. Tear breakup is again evident at about 33 s during which time the surrounding uniform tear film thins from 3.5 to 2.2 μm due to evaporative loss.

As shown in Fig. 5A, the temperature of the evaporating tear-film surface is lower than that of the eye at 35 °C, but only so by less than 0.01 °C. The thinness of the tear film presents minimal heat-transfer resistance so the cornea and tear temperatures are nearly equal. All heat necessary to evaporate the tear is obtained from the eye. The surface temperature of the instability recession is slightly warmer than that of the surrounding tear film due to the thinness of the depression and to the resulting lower conductive heat-transfer resistance. The temperature of the trough floor reaches that of the eye at tear rupture, 35 °C in Fig. 5B. In Eq. (4), we neglect the enthalpy carried by the warm weeping flow into the tear film from the cornea because osmotic-weeping flow accounts for a small fraction of the volume change of the tear film compared to that arising from evaporation (i.e., $J_e >> J_w$).

The important finding from Fig. 5 is that the temperature of the tear-film surface is that of the cornea with negligible difference. Hence, in the calculations presented below, we no longer report $T_S(x,t)$. The temperature at the corneal epithelium is assumed constant in our model, which potentially underestimates the temperature variation in the z-direction of the tear film. In the future, an extended heat-transfer model including that of the anterior eye (cornea and aqueous humor) [77] can be incorporated to examine more carefully temperature effects on tear-film stability.

Fig. 6A reveals a fascinating salt-osmolarity spike at the instability center ($x = 0$). Here the salt concentration increases from 300 mOsM to 545 and 850 after 10 and 20 s, respectively, and soars to 1534 mOsM after a 33-s interblink corresponding to tear-film breakup. In regions

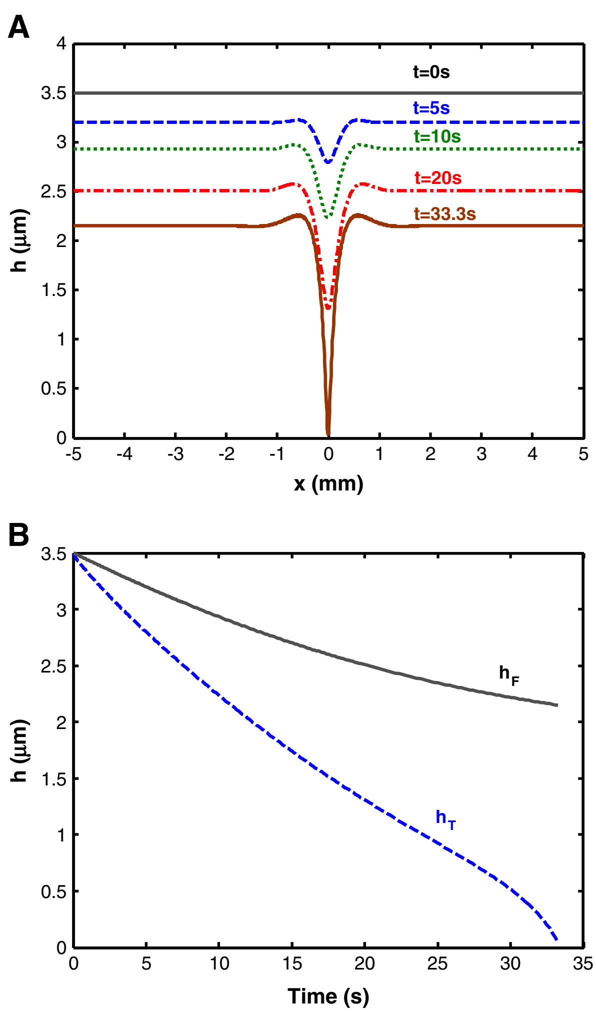

Fig. 4. Dynamics of tear-film thickness under typical indoor conditions (Table 1). h_T and h_F represent tear-film thicknesses at $x = 0$ and $x = \pm 5$ mm, respectively.

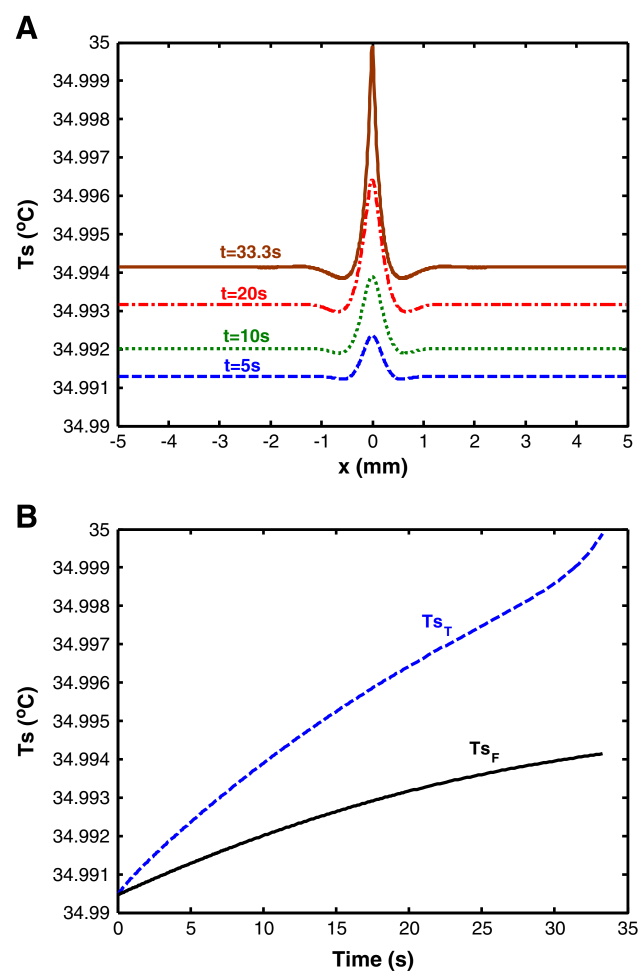

Fig. 5. Dynamics of tear-film temperature at the air/aqueous interface under typical indoor conditions (Table 1). Ts_T and Ts_F represent interface temperatures at $x = 0$ and $x = \pm 5$ mm, respectively.

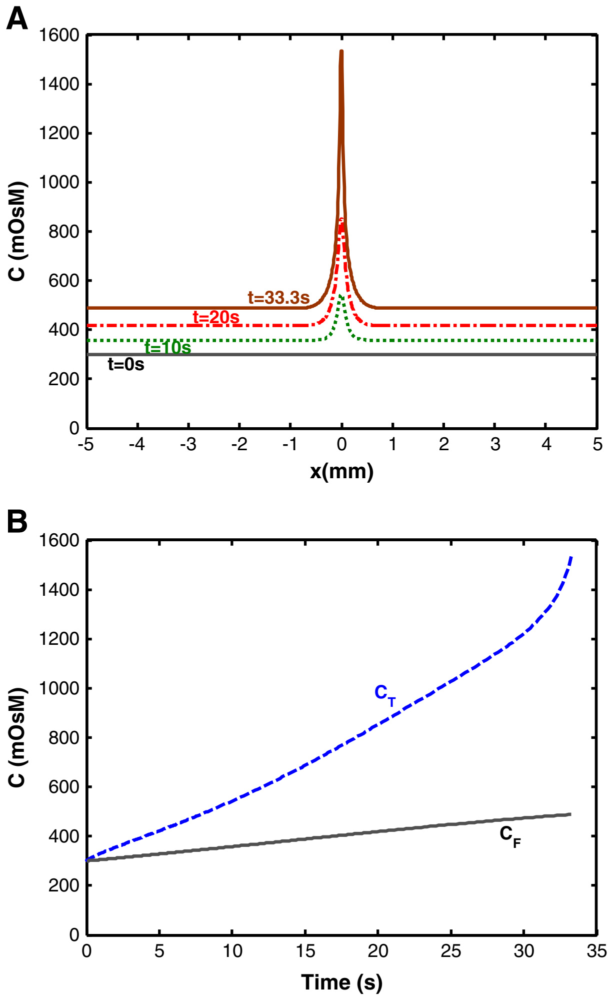

Fig. 6. Dynamics of tear-film osmolarity under typical indoor conditions (Table 1). C_T and C_F represent tear-film osmolarity at $x = 0$ and $x = \pm 5$ mm, respectively.

surrounding the trough, the increase in osmolarity remains strong, but more modest, from 300 mOsM to 360, 420, and 488 mOsM over the same respective time period. The thinner is the tear film underneath the trough, the larger is the relative increase in salinity due to evaporative-water loss. Conversely, curvature-driven healing flow draws in water from the surroundings as does weeping flow from the cornea. These two flows partially offset the evaporative osmolarity increase. Over that left behind from water evaporation, curvature-driven flow supplies additional salt to the growing trough. The only escape for salt from the deepening trough is back diffusion against the two convective flows. For realistic diffusion coefficients, salt back diffusion lowers the local osmolarity enough to prevent aqueous osmotic inflow from stabilizing the instability. Nevertheless, diffusion is too slow to prevent salt accumulation within the tear-rupture depression; a local salinity "hot spot" emerges [65].

Fig. 6B compares the salinity history in the furrow of the trough (dashed line) to that in the surrounding tear (solid line) corresponding to the salinity profiles in Fig. 6A. Salt content of the encompassing tear slowly increases, whereas that in the tear underneath the instability rises dramatically. At the point of tear rupture, about 33 s, trough salinity abruptly ends at about 1534 mOsM. Once the tear film disappears leaving behind a dry spot, aqueous salt concentration is no longer well defined in the calculation.

The most important finding from Figs. 4–6 is that tear-film breakup due to elevated evaporation below a lipid-film rupture is physically reasonable. The parameters underlying Figs. 4–6 fall within clinically observed trends. To our knowledge, this is the first physically consistent quantitative explanation for the formation of black streaks and/or spots during a human interblink. The proposed model for breakup, however, is not universal. First, a pre-TFLL rupture is demanded resulting in a relatively large rate of water evaporation. Second, the initial blink-deposited precorneal tear film must be perched and relatively thin, and third, no other healing flows are present except those due to curvature and osmotic weeping. We investigate briefly the roles of several pertinent physical parameters to gain insight into the generality of evaporation-induced tear-film rupture.

4.2. Healing flow

Fig. 7 illustrates the roles of curvature-driven and weeping flows in preventing evaporative tear-film rupture. With both curvature-induced and weeping-induced flows, rupture time in Fig. 7 curve C is that of Figs. 4–6 or 33 s. If curvature flow is prevented by setting the tear-film surface tension to zero in Fig. 7 curve A, then rupture occurs quickly in 5.5 s. Conversely, blocking weeping flow by setting the corneal water permeability to zero in Fig. 7 curve B has much less of an effect. Breakup occurs in about 19 s. We conclude that healing flow arising from curvature outweighs significantly that arising from weeping flow through the cornea.

4.3. Initial tear thickness

The role of the initial precorneal tear thickness on rupture is illustrated in Fig. 8A. Reported average tear-film thicknesses under normal conditions vary between 1.6 and 7.3 μm [10] with more recent interferometric measurements favoring thinner films [56]. With all other parameters identical to those in Fig. 4, a 7-μm tear film does not rupture within a measureable interblink time, whereas a 2-μm tear film ruptures in 10 s. Eventually, the 7-μm tear film ruptures in Fig. 8A, but long after a human interblink can be sustained. Tear rupture within an observable interblink time due to the proposed evaporative mechanism depends strongly on the initial tear-film thickness: only thin tear films rupture.

No mechanism is yet available to account for black spots or streaks in thick precorneal tear films. Nevertheless, Fig. 8B shows that there is a substantial increase in salinity within the slowly growing trough. Salt content in an initial 300-mOsM tear film rises to 580 mOsM after 35 s under the most slowly deepening instability in Fig. 8 ($h_o = 7$ μm). For a tear film with several growing, but not completed,

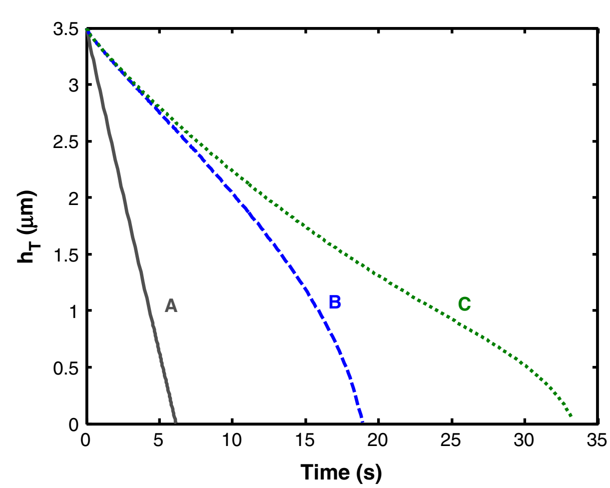

Fig. 7. Effect of surface tension (γ) and corneal water permeability (P_c) on preventing localized tear-film breakup. (A) $\gamma = 0$, $P_c = 2.34 \times 10^{-10}$ m/s/mOsM; (B) $\gamma = 4.5 \times 10^{-2}$ N/m, $P_c = 0$ and (C) $\gamma = 4.5 \times 10^{-2}$ N/m, $P_c = 2.34 \times 10^{-10}$ m/s/mOsM. All other parameters are given in Table 1.

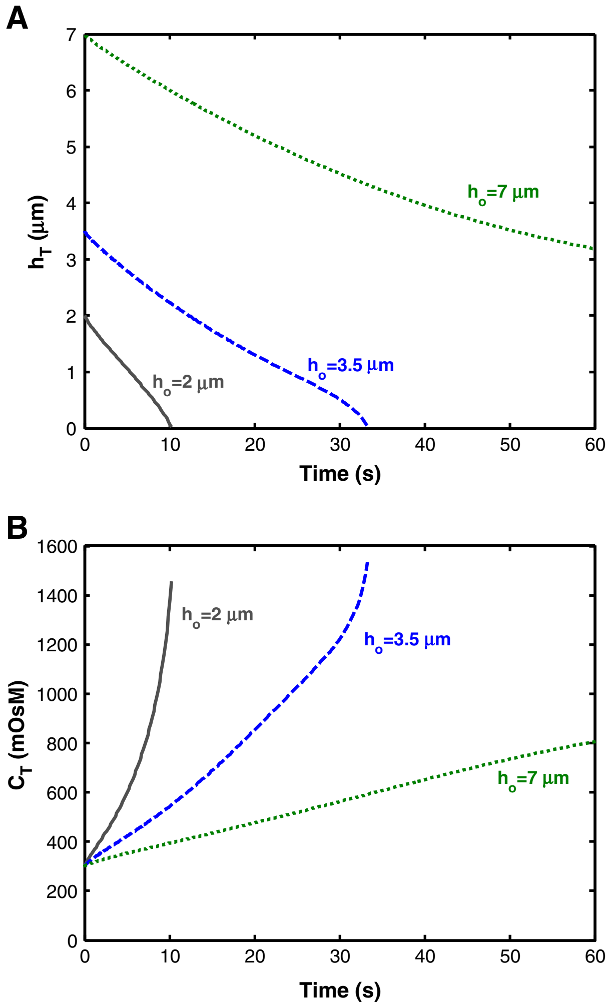

Fig. 8. Dynamics of tear-film thickness and osmolarity at the center of TFLL breakup ($x = 0$) with various initial tear-film thicknesses (h_o). All other parameters are given in Table 1.

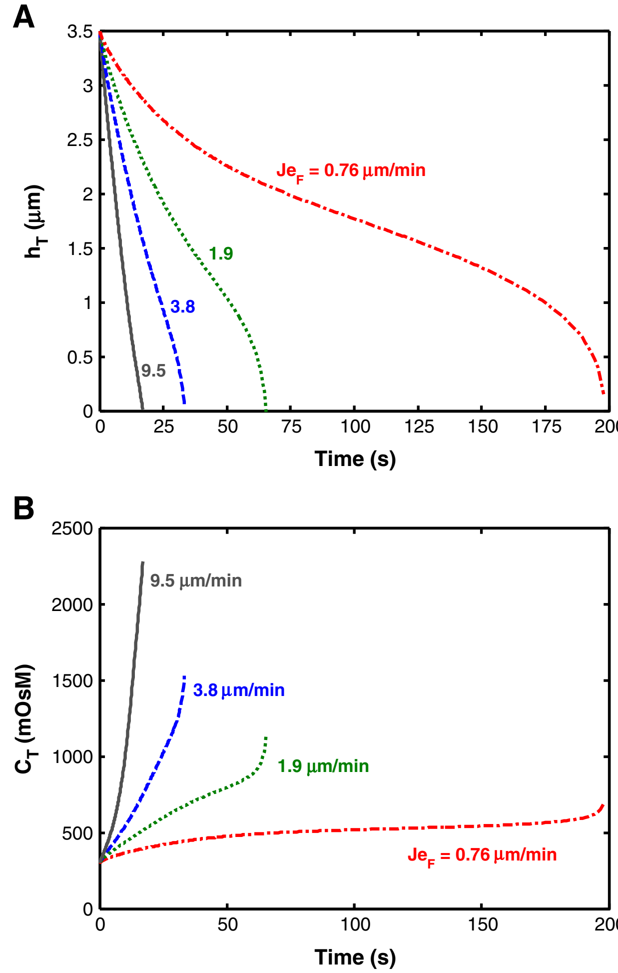

Fig. 9. Dynamics of tear-film thickness and osmolarity at the center of TFLL breakup ($x = 0$) with various background evaporation rates of J_{eF}. The evaporation rate at the center of TFLL breakup, J_{eT}, is maintained at 38 μm/min for all conditions. All other parameters are given in Table 1.

instabilities, the cornea is exposed to a number of salinity hot spots and, hence, possible eye discomfort [65]. Human subjects who exhibit thinner tear films, such as evaporative dry-eye patients, are exposed to higher general salinities in addition to hot spots even when tear breakup is not observed. When tear breakup is observed in such subjects, much higher salinity hot spots exist.

4.4. Tear-film evaporation rate

The calculations presented above correspond to a 90% reduction in evaporation rate outside the instability due to an intact 100-nm thick TFLL (see Fig. 3). Earlier studies on rabbits demonstrated that complete removal of the lipid layer increased evaporation rate from 4-fold [52] to as high as 20-fold [53]. Measurements conducted on human subjects showed that evaporation rates significantly increased, by about four times, in patients with no detectable lipid layer (<10 nm) [78]. Tear-film evaporation rate under normal conditions demonstrates considerable variation [55–58]. To address the role of TFLL evaporation reduction, the background evaporation rate was altered while keeping the same elevated evaporation rate at the center of tear film where the lipid layer is absent, (i.e., $J_{eT} = 38$ μm/min). Fig. 9 shows the dynamics of tear-film thickness and osmolarity at the center of TFLL breakup with various evaporation reductions by the intact 100-nm thick lipid layer. By increasing evaporation reduction by 75%, 90%, 95%, and 98%, the evaporation rate of the tear film away from lipid-deficient region, J_{eF}, decreases as 9.5, 3.8, 1.9, and 0.76 μm/min, respectively. As illustrated in Fig. 9A, tear-film breakup time decreases with increased J_{eF} even though J_{eT} remains constant. With a small background evaporation rate of 0.76 μm/min, or that reported with the "fluid-capture" goggle method in a stagnant air [57,58], the instability-trough thickness only decreases from 3.5 to 2.1 μm after a 60-s interblink. No tear-film rupture is predicted with a 0.76 μm/min background tear-film evaporation rate. Conversely, tear-film breakup time shortens to ~60 s when the background evaporation rate increases to 1.9 μm/min. Thus, tear rupture only occurs with sufficiently high evaporation rate from the undisturbed tear film. Fig. 9B reveals that for reduced evaporation rates salinity hot spots still form at the region of instability.

4.5. Wind speed

The evaporation rate of pure water at the nadir of a deepening tear instability is not a fixed value but depends on, among other parameters, environment air flow and relative humidity. Higher wind speeds reduce the mass-transfer resistance in the air phase and lead to higher evaporation rates. In comparison to Fig. 4 for a perpendicular-directed wind of 0.3 m/s, Fig. 10A reports the effects of different perpendicular-directed wind speeds: 0.1, 0.3, 1 and 10 m/s that represent sequentially "sitting/reading", "working(indoor)", "walking", and "bicycling", respectively [76,79]. Mass-transfer coefficients for water vapor in air are estimated from impinging-jet flow [80]. Resistance to evaporation, $R_G = 1/k_m$, is thus estimated as 90.9, 51.5, 28.7 and 9.1 s/m for sitting,

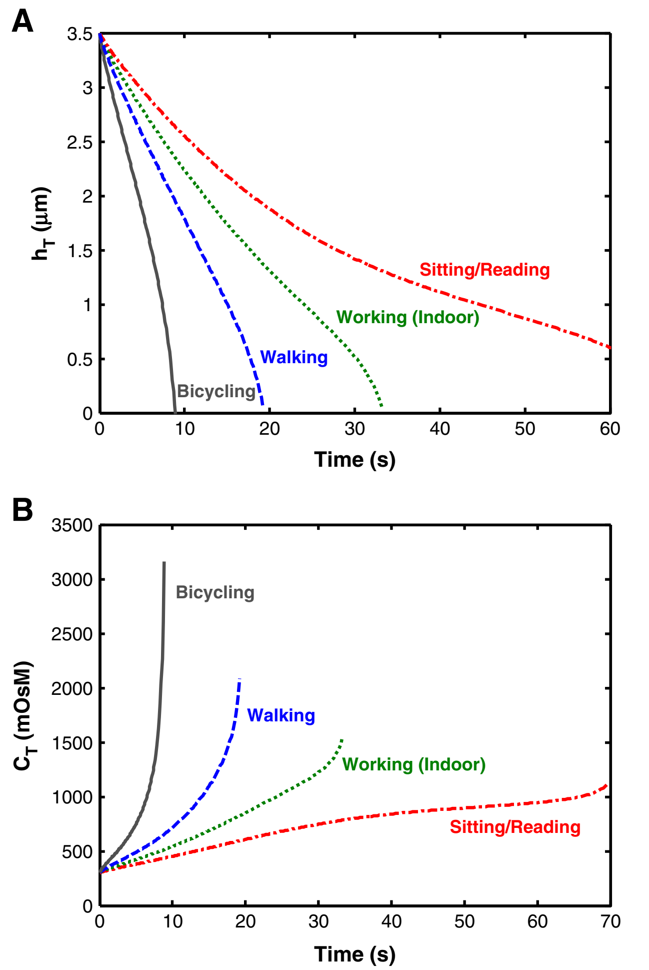

Fig. 10. Dynamics of tear-film thickness and osmolarity at the center of TFLL breakup ($x = 0$) with various wind speeds in ambient air. The "sitting", "working", "walking" and "bicycling" conditions represent wind speeds of 0.1, 0.3, 1 and 10 m/s, respectively, giving corresponding mass-transfer resistances (R_G) of 90.90, 51.55, 28.74, and 9.08 s/m. All other parameters are given in Table 1.

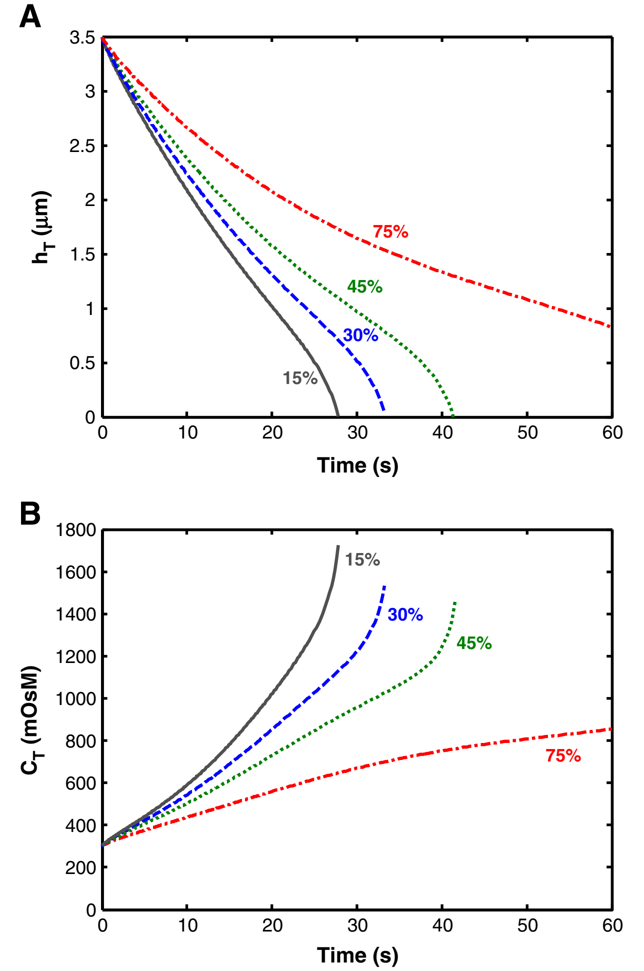

Fig. 11. Dynamics of tear-film thickness and osmolarity at the center of TFLL breakup ($x = 0$) with various relative humidities in ambient air. All other parameters are given in Table 1.

working, walking, and bicycling [79,80] giving corresponding pure-water evaporation rates of 21.5 μm/min (sitting), 38.0 μm/min (working), 68.1 μm/min (walking), and 215 μm/min (bicycling). For fixed water permeability in the TFLL corresponding to Fig. 4 ($D_k K_w = 2.2 \times 10^{-10}$ m^2/s), the background evaporation rates are 3.5, 3.8, 4.0, and 4.1 μm/min for sitting, working, walking and bicycling, respectively. Wind speed clearly plays an important role in controlling rupture times, especially at higher speeds. During sitting or with minimal activity, tear rupture can be forestalled. Nevertheless, Fig. 10B re-emphasizes that even without tear breakup, significant salinity hot spots grow in the tear under any growing instability.

4.6. Relative humidity

Reduced air humidity exacerbates dry-eye symptoms [81,82]. The presumption is that low relative humidity increases the evaporation rate thereby lowering BUT and increasing tear salinity [81,82]. Fig. 11A confirms this presumption. When the relative humidity decreases in Fig. 11A from 30%, that in Fig. 4, to 15%, representing an airplane cabin or an arid environment, evaporative-driven rupture time decreases from 33 to 28 s, a measureable effect. Conversely, increasing the relative humidity to 75% staves-off interblink tear rupture. As illustrated in Fig. 11B, however, major salinity hot spots still arise even when there is no interblink tear rupture.

4.7. Spot instability

The Cartesian geometry adopted in all figures above represents a trough instability or a black streak. Black-spot or dimple instabilities are also common, for example, as evidenced in Fig. 1. To mimic a black spot, we consider an axisymmetric cylindrical coordinate system (i.e., r and z) with a circular TFLL rupture as detailed in Eqs. (A19)–(A26). Comparison between instability thickness for black-spots (solid lines) and black-streaks (dashed lines) is highlighted in Fig. 12 for two different TFLL-rupture standard deviations of 100 and 200 μm. For a given rupture size, black streaks grow more quickly than do black spots, all else being equal. This finding is reasonable because a circular depression in the tear film induces relatively more curvature-driven healing flow from the instability perimeter compared to that for a linear trench where there is no healing flow from the direction parallel to the trench (y-direction). More healing flow waylays rupture. Fig. 12 also shows that increasing the size of the instability decreases BUT. A larger trough or dimple increases the resistance for curvature-driven healing flow because more fluid must be drawn into the depression center from a longer distance away. The results in Fig. 12 suggest a wide variety of rupture patterns as differing-shaped growing depressions merge and expand.

4.8. Surface tension

As mentioned earlier, curvature-driven healing is the dominant flow preventing tear-film rupture due to evaporation. Infill volumetric

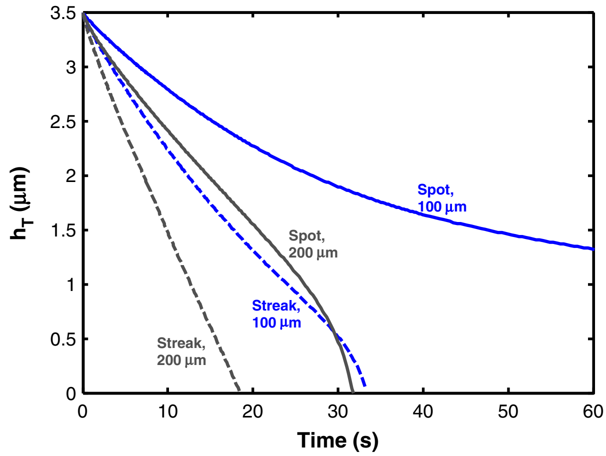

Fig. 12. Dynamics of tear-film thickness at the center of TFLL breakup ($x = 0$) with various sizes of TFLL rupture in Cartesian (streak) or cylindrical (spot) coordinates. All other parameters are given in Table 1.

flux is proportional to the surface tension at the aqueous/air interface. Fig. 13 shows the effect of surface tension on the center-thickness dynamics of a streak instability. Clearly, BUT decreases as the surface tension decreases. The surface tension of normal tear is about 2/3 of that of pure water/air interface or 45 mN/m [83,84]; Clinical observations suggest that the average surface tension of tear is higher for dry-eye patients [85]. Fig. 13 indicates that during evaporation-driven tear-film thinning, higher surface tension enhances curvature-driven healing flow and forestalls tear-film instabilities. It is sometimes argued that the lipid layer stabilizes the tear film against rupture by lowering the surface tension and, hence, lowering the free energy of the tear film [18,86]. Fig. 13 argues against this supposition: lower tear surface tension encourages breakup by slowing healing flow.

As discussed in Section 2, surface-tension gradients (i.e., Marangoni flows) stabilize against rather than induce tear-film rupture. We assume a constant tear-film surface tension. This approximation is consistent with recent *in vivo* interferometry and fluorescein-quenching experiments concluding that evaporation, not tangential flow, is the main factor driving tear-film thinning [38,42]. We also do not account for the dynamics of TFLL rupture, or for the presence of proteins and mucins in the aqueous layer that might influence tear physical properties. Presumably these effects are secondary to the evaporative origin of the proposed evaporative instability.

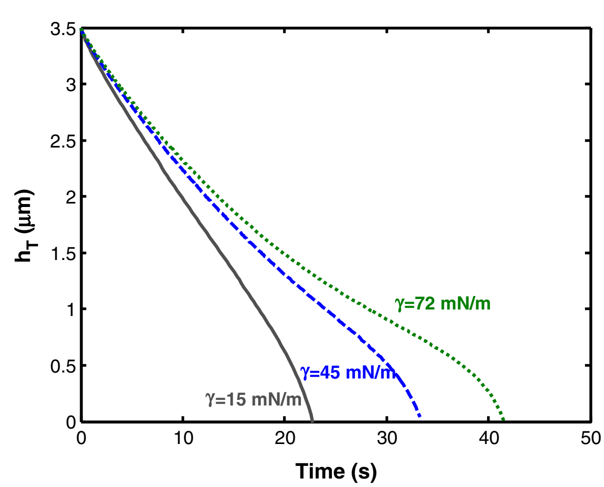

Fig. 13. Dynamics of tear-film thickness at the center of TFLL breakup ($x = 0$) with various surface tensions, γ, at the tear-film interface. All other parameters are given in Table 1.

4.9. Epithelial disjoining forces

In all figures above, tear rupture occurs when the trough or dimple center reaches zero thickness forming a dry streak or dry spot. The epithelial/tear interface, however, is impregnated with membrane-bound glycogalyx mucin and possibly interspersed with soluble gel-forming mucins, both of which are highly water liking [11–13]. The overriding soluble mucin molecules keep the epithelial surface strongly water wet [11–13] so that dry regions void of liquid are unlikely. To account for the strong water-wetting nature of the epithelium, we introduce a repulsive disjoining force obeying the Hamaker functionality, $\Pi = -A/6\pi h^3$ with A negative. Because the Hamaker thin-film force is infinite for a zero-thickness film, mechanical rupture of water layers is prevented in the range of these forces, approximately 100-nm away from the epithelium. Consequently, a dry patch is theoretically not permitted. A 100-nm unbroken tear layer compared to a broken one still appears black in macroscopic BUT experiments and is not possible to detect under fluorescein observation. Further, strong water binding by the thin glycocalyx region of the anterior epithelial cells likely impedes, if not completely prevents, water evaporation [71,87,88]. In our model, the presence of disjoining pressure at the trough center affects the infill volumetric flux, u, in Eqs. (1) and (5), as detailed in Appendix A. In addition, the vapor pressure of water at the interface is also affected when the film thickness decreases to within the range of the disjoining force, as shown in Eq. (2). Fig. 14 demonstrates how a Hamaker disjoining force prevents tear-film rupture. As in Fig. 4, when

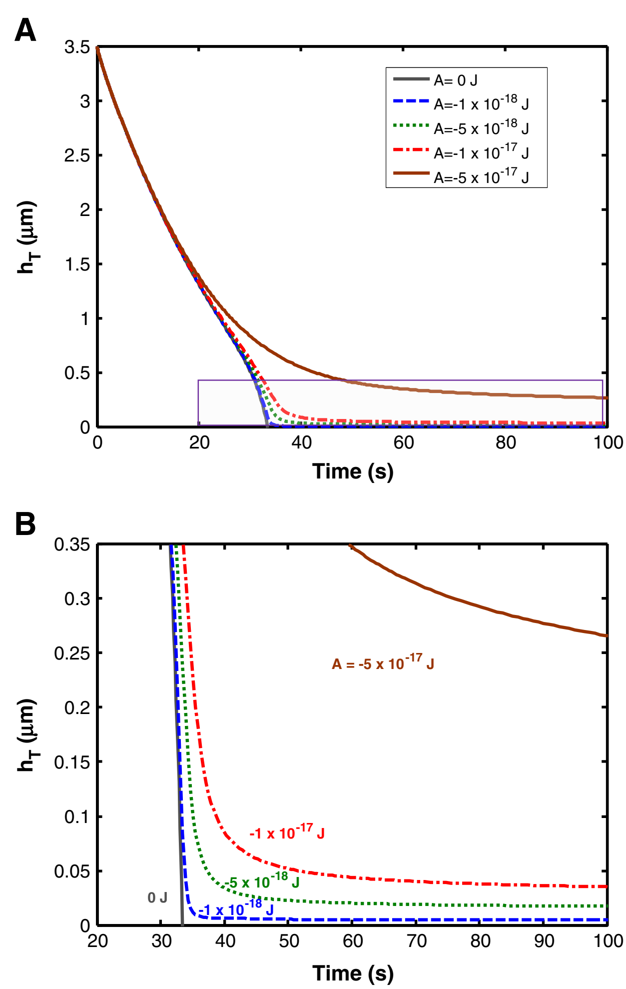

Fig. 14. Dynamics of tear-film thickness at the center of TFLL breakup ($x = 0$) with various repulsive Hamaker constants. (B) is the enlargement of (A) at long times. All other parameters are given in Table 1.

no disjoining pressure is considered (i.e., $A = 0$), the film thickness reaches zero in 33 s. When $A = -10^{-18}$ J, film thinning is retarded at a thickness of around 50 nm and eventually stabilizes at 4.5 nm. This final constant film thickness rises as the repulsive Hamaker dispersion force increases.

Fig. 15 shows the corresponding dynamics of tear-film osmolarity at the trough center for various repulsive Hamaker constants. Disjoining pressure prevents the film thickness from reaching zero where osmolarity approaches infinity, and, thus, stabilizes the final osmolarity in a constant thickness film. Increased magnitude of repulsive Hamaker constants lead to larger stabilized film thicknesses (see Fig. 14) and correspondingly lower stabilized osmolarties. When the repulsive Hamaker constant is small in magnitude, e.g. 10^{-18} J, a bulge in osmolarity arises. In the case of zero disjoining force, a spike happens in an instant, and the osmolarity approaches infinity. However, with a finite disjoining pressure to prevent tear-film rupture, the osmolarity burst is damped by osmotic-driven weeping water flow through the corneal epithelium.

Fig. 16 shows the evaporation rates at the center of a trough instability (where the TFLL is absent) normalized to the initial evaporation rate at time zero. The evaporation rate slightly increases (<0.1%) during the tear-film thinning before the film reaches submicron thicknesses. This minor increase is due to the small increase of surface temperature during tear-film thinning, as shown in Fig. 5. However, the evaporation rate decreases when the film reaches the region where the disjoining force becomes significant. As discussed earlier, a repulsive disjoining pressure lowers the vapor pressure over that of a thick, flat film, and thus, decreases the evaporation rate. Fig. 16 indicates that the Hamaker force has a negligible effect on evaporation rate when the magnitude of A is larger than 10^{-17} J. The reason is that disjoining pressure prevents tear-film rupture mainly through enhancing healing flow and not through reducing the evaporation rate. Thus, film thinning is prevented by increased healing flow, and the trough center does not fall to film thicknesses where the evaporation rate is significantly affected by thin-film forces.

5. Discussion

We do not include the possible stabilizing effect of classical surfactant-gradient Marangoni stresses [20,21,23–25,29–37] during black-streak (spot) formation. The TFLL is not an adsorbed surfactant monolayer at an air/water interface. Rather, it is a 100-nm or less duplex oil film consisting of two interfaces (air/oil and water/oil) with a viscous waxy dispersion sandwiched between [89]. The lipid/water interface of the TFLL is laden with surfactant phospholipids and partially denatured protein [89]. Approximating the TFLL as a surfactant monolayer adsorbed at the air/water surface is unrealistic.

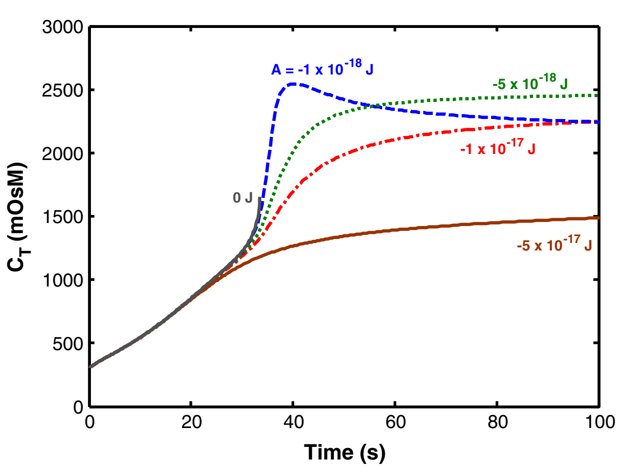

Fig. 15. Dynamics of tear-film osmolarity at the center of TFLL breakup ($x = 0$) with various repulsive Hamaker constants. All other parameters are given in Table 1.

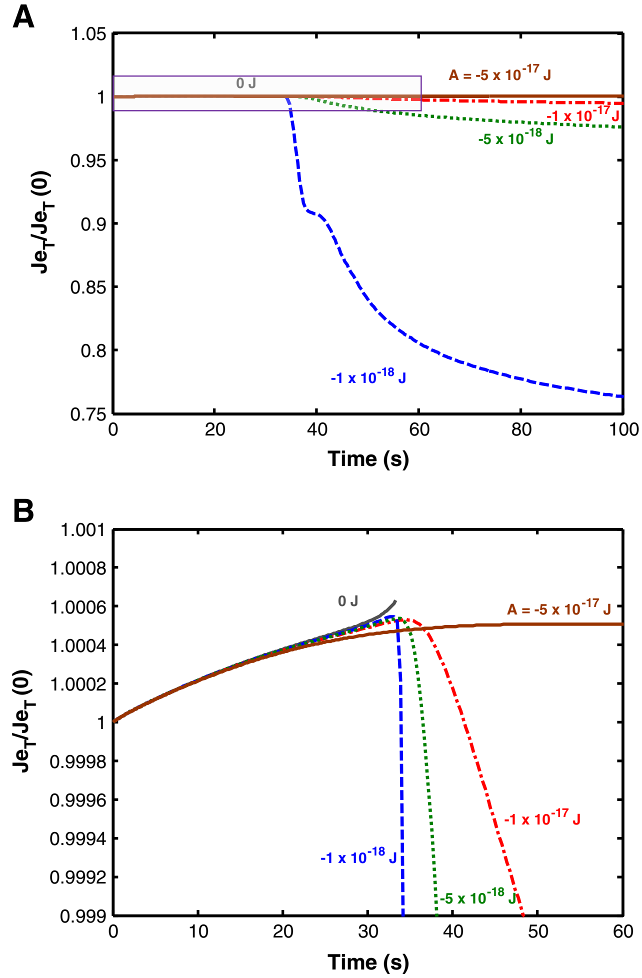

Fig. 16. Normalized evaporation rate, $J_{eT}/J_{eT}(o)$, at the center of the TFLL breakup ($x = 0$) with various Hamaker constants. $J_{eT}(o)$ is 38 μm/min. (B) is the enlargement of (A) at short times. All other parameters are given in Table 1.

The chosen duplex-film lipid-layer profile, $L_L(x)$, in Fig. 3 has no influence on the rate of tear streak/spot growth other than to control the local evaporation rate. However, the assumed $L_L(x)$ profile is consistent with attractive (conjoining) thin-film forces that drive lipid flow away from the TFLL rupture region. Resulting lipid flow drags underlying tear outwards from the growing tear dimple providing an additional stabilizing flow over those from curvature- and osmotic-driven healing flows. A complete analysis of evaporative-driven tear-film rupture is beyond the scope of the current feasibility analysis.

Since tear rupture commences by the appearance of individual spots and/or streaks, our proposed 1-D analysis of isolated rupture events is pertinent for establishing the feasibility of evaporative-driven tear breakup. Interacting spots or streaks that occur later in the rupture process require a 2-D analysis.

6. Conclusions

We demonstrate that an evaporation-driven tear-film rupture mechanism is a physically consistent explanation for the formation of black streaks and spots in the human tear film during an interblink. Elevated evaporation rate in a lipid-deficient spot drives the instability. With reasonable TFLL breakup sizes, shapes, and evaporation rates, tear-film breakup occurs in 10 ~ 45 s under normal environmental conditions, but relatively higher tear evaporation rates are needed. Predicted roles of wind speed and relatively humidity on tear-film stability compare well with clinical observations. More importantly, locally elevated evaporation leads to hyperosmolar spots in the tear film and, hence, vulnerability to epithelial irritation. In addition to evaporation rate, tear-film instability depends significantly on the strength of healing flow from the tear outside the breakup domain. Contrary to common belief, low tear surface tension reduces curvature-driven healing flow and promotes tear breakup. For the first time, we quantitatively relate environmental conditions to human tear-film instability.

Acknowledgment

This work was partially funded by Alcon Corporation under Contract 022466-003 to the University of California.

Appendix A. Mathematical model for tear-film evolution

Since the thickness of tear film is three orders of magnitude smaller than the diameter of the precorneal tear film, mass conservation for water in the thin film in Eq. (1) is based on lubrication theory accounting for flow in the x-direction, evaporation, and osmotic water influx [72,73].

The evaporative flux, J_e, depends on the gas-phase mass-transfer resistance, R_G, the lipid film mass-transfer resistance, R_F, and the water vapor concentration driving force between the environment and the tear-film surface, as described in Eq. (2) of the text. The mass-transfer coefficient of the air phase, k_m, is estimated by assuming impinging-jet flow with a stagnation region near the tear-film surface and a uniform laminar flow with known speed exiting the nozzle located infinitely far away from the tear film [80]. As shown in Fig. 3, $L_L(x)$ is varied in a Gaussian fashion [64] to represent a locally absent or deficient lipid layer that increases evaporation according to the change of R_F. The intact lipid layer is assumed to reduce evaporation rate of water by 90% [53], i.e., the evaporation rate is 10-fold higher at the region where lipid layer is absent than that at the region covered by a complete lipid layer with initial evaporation rate of 3.8 μm/min at a relative humidity of 30% [56]. Water permeability in the lipid layer is 2.16×10^{-10} m^2/s [60].

To establish the Kelvin correction in Eq. (2), local equilibrium is assumed so that the chemical potential of water, μ, in the liquid film and gas phase is identical

$$\mu_G = \mu_L = \mu\left(T, h, \frac{\partial^2 h}{\partial x^2}\right) \tag{A1}$$

The chemical potential of both the gas and liquid phases depends on temperature, and also on interface curvature (surface tension) and film thickness (conjoining/disjoining pressure). To determine these latter two dependencies, the Gibbs–Duhem equation is written for the liquid phase at constant temperature as

$$-\tilde{V}_L dP_L + d\mu_L = 0, \qquad \text{const}\, T \tag{A2}$$

where $\tilde{V}_L$ is liquid-water molar volume and P_L is the liquid pressure. Thus, from Eq. (A1) at constant temperature

$$d\mu = d\mu_L = \tilde{V}_L dP_L = \frac{1}{\tilde{\rho}_L} dP_L, \qquad \text{const}\, T \tag{A3}$$

Upon integrating both sides of Eq. (A3) between a zero curvature and a finite-curved interface and by replacing μ_L by μ_G based on Eq. (A2) we find that

$$\tilde{\rho}_L\left(\mu_G - \mu_G^{sat}\right) = P_L - P_w^{sat} = \left(P_G - P_w^{sat}\right) + (P_L - P_G), \qquad \text{const}\ T \tag{A4}$$

The first term on the far right of Eq. (A4) is generally neglected because it is much smaller than the second term. Upon assuming ideal-gas behavior, Eq. (A4) is rewritten as

$$\tilde{\rho}_L R_g T \ln \frac{P_G}{P_w^{sat}} = P_L - P_G \tag{A5}$$

The augmented Young–Laplace equation for a thin liquid film with small surface curvature is given by [26,27,90]

$$P_G - P_L = \gamma \frac{\partial^2 h}{\partial x^2} + \Pi \tag{A6}$$

where γ is the surface tension at the interface, and Π is the conjoining/disjoining pressure. We take $\Pi = -A/6\pi h^3$ between two flat interfaces [26,27]. Substitution of Eq. (A6) into Eq. (A5) gives

$$P_G = P_w^{sat}(T) \exp\left(-\frac{1}{\tilde{\rho}_L R_g T}\left(\gamma \frac{\partial^2 h}{\partial x^2} - \frac{A}{6\pi h^3}\right)\right) \tag{A7}$$

For a repulsive disjoining force, A is negative. Since the surface-tension term in the exponential is typically negligible, the vapor pressure decreases when the film thickness decreases to the region where the Hamaker thin-film force becomes significant. This result is equivalent to Kelvin's equation for vapor-pressure lowering under a curved bubble interface [26,27]. Eq. (A7) explains the exponential (or Kelvin) correction to the saturation vapor pressure in Eq. (2) of the main text.

We now write the osmotic water volumetric flux as

$$J_w(x,t) = P_c[C(x,t) - C_0] \tag{A8}$$

where P_c is the osmotic permeability (m/s/mOsM) of the cornea or conjunctiva to water, and $C(x,t)$ and C_0 are the tear-film and serum molar salt concentrations, respectively [69]. Although the fundamental molecular physics of weeping flow is not fully understood, Eq. (A8) provides a reasonable estimate [69,70]. Corneal water permeability measured on mice is about 1.97×10^{-10} m/s/mOsM (1.1×10^{-5} m/s) [91]. Estimates for humans are 2.34×10^{-10} m/s/mOsM (1.3×10^{-5} m/s) [64] and 4.0×10^{-10} m/s/mOsM when hydraulic, osmotic and electro-osmotic flows are combined [69].

We must also conserve salt (i.e., primarily sodium chloride) in the aqueous tear film assuming that the salt concentration varies only in the x-direction due to diffusion and convective mass transport. The characteristic time for diffusion of salt in the z-direction is $\tau_{sz} = h^2/D$, where D is the diffusion coefficient of salt in water. In a 3-μm-thick tear film, $\tau_{sz} \sim 0.01$ s, assuring a well-mixed condition in the z-direction. Local conservation of salt then reads

$$\frac{\partial(hC)}{\partial t} = -\frac{\partial}{\partial x}\left(-Dh\frac{\partial C}{\partial x} + uCh\right) \tag{A9}$$

If we apply the product rule to the time derivative and substitute Eq. (1) into (A9), the effects of evaporation and osmotic water influx on the salt concentration become clearer as stated in Eq. (5).

In a lubrication analysis, the augmented Young–Laplace equation relates the anterior interface curvature to the liquid pressure, including conjoining/disjoining pressure between the two interfaces of the tear film. Assuming small curvatures, we write the following expression for water flow in the aqueous layer

$$u = \frac{h^2}{12\mu}\left(-\frac{\partial P_L}{\partial x}\right) = \frac{h^2}{12\mu}\left(\gamma \frac{\partial^3 h}{\partial x^3} + \frac{\partial \Pi}{\partial x}\right) \tag{A10}$$

where P_L is the liquid pressure, μ is the tear viscosity, γ is the surface tension of aqueous tears, and Π is the conjoining/disjoining pressure in the film. Eq. (A10) is used to eliminate the flow velocity from Eqs. (1) and (5).

The last conserved quantity is the energy of the tear film. We assume that heat conduction from the epithelial surface provides the energy for evaporation, so the tear temperature varies in the z-direction. Because the evaporative flux varies with x, we also expect tear temperature to depend on x. Then the thermal balance within the tear film is

$$\frac{\partial T}{\partial t}+u\frac{\partial T}{\partial x}=\alpha\left(\frac{\partial^2 T}{\partial x^2}+\frac{\partial^2 T}{\partial z^2}\right) \tag{A11}$$

Since the thickness of tear film is much smaller than its diameter, scaling reduces Eq. (A11) to

$$\frac{\partial^2 T(x,z)}{\partial z^2}=0 \tag{A12}$$

Eq. (A12) demands a linear temperature profile in the z-direction at each x even though the temperature changes with x-position and time.

Boundary conditions for the thermal balance are,

$$T(t,x,0)=T_e, \tag{A13}$$

and

$$-k_w\frac{\partial(T(t,x,h))}{\partial z}+U[T_\infty-T(t,x,h)]=\frac{J_e}{\rho_w}\Delta\hat{H}_v \tag{A14}$$

where U is the heat transfer coefficient of air that depends on geometry and air flow, k_w is the thermal conductivity of the aqueous tear film, and $\Delta\hat{H}_v$ is the specific latent heat of vaporization of water. Thermal resistance of the TFLL is neglected. Since the mass-transfer coefficient is known for impinging-jet flow [80], the convective heat-transfer coefficient in the air is correlated by the Chilton-Colburn analogy that relates the Nusselt number to the Sherwood, Prandtl, and Schmidt numbers as [92]

$$Nu=Sh\left(\frac{Pr}{Sc}\right)^{\frac{1}{3}} \tag{A15}$$

Thus, given the mass-transfer coefficient, k_m, the heat-transfer coefficient of air is determined as

$$U=k_T\frac{k_m}{D_{water/air}}\left(\frac{Pr}{Sc}\right)^{\frac{1}{3}} \tag{A16}$$

where k_T is the thermal conductivity of air, and $D_{water/air}$ is the diffusion coefficient of water in air. At 25 °C, assuming the wind speed in the air is 0.3 m/s, k_m is estimated as 1.94×10^{-2} m/s [80], Pr and Sc for air are 0.7 and 0.64, respectively. k_T is 2.63×10^{-2} W/m/K, and $D_{water/air}$ is 2.53×10^{-5} m^2/s [92]. Thus, U is estimated to be 20.7 (W/m$^2\cdot$K).

The first boundary condition in Eq. (A13) assumes a constant epithelial surface temperature, T_e. The second boundary condition in Eq. (A14) describes local conservation of thermal energy at the air/tear-film interface, including heat influx from the tear film, heat loss to the environment, and heat loss to evaporation during the interblink. By solving Eqs. (A12)–(A14), we obtain the tear-film surface temperature, T_S, as given in Eq. (4) of the main text.

Six chosen unknowns (h, C, u, T_S, J_e, and J_w) in six equations (Eqs. (1), (2), (4), (5), (A8), and (A10)) are solved simultaneously to yield the tear-film dynamics. Among these, Eqs. (1) and (5) are partial differential equations, whereas Eqs. (2), (4), (A8), and (A10) are algebraic. Eq. (A10) contains a third-order spatial derivative in film thickness. To apply Eq. (A10) numerically, we introduce a new variable

$$H=\frac{\partial^2 h}{\partial x^2} \tag{A17}$$

By substituting Eq. (A17) into Eq. (A10), we obtain seven coupled nonlinear equations for seven unknown variables each depending on x and t: h, H, C, u, T_S, J_e, and J_w. Eqs. (1), (5), (A10), and (A17) become first or second-order nonlinear partial differential equations. The corresponding boundary conditions for these equations are,

$$\frac{\partial h}{\partial x}=0;\quad \frac{\partial C}{\partial x}=0;\quad \frac{\partial u}{\partial x}=0\ \ and\ \ \frac{\partial H}{\partial x}=0\ \ at\ \ x=\pm L \tag{A18}$$

where L is the radius of tear-film in this model. The boundary conditions demand no flow in x-direction at the edge of the tear film. The edge of the film is viewed as infinitely far from the center. The physical reason for these boundary conditions is that the precorneal tear film is "perched" by the black lines formed immediately after tear-film deposition due to capillary suction from menisci at the lid margins. No flow exchange occurs across the black lines between blinks [66,67]. The initial tear film is flat ($H(x,0)=0$; $u(x,0)=0$) with thickness h_o; the initial osmolarity in the tear film is the serum osmolarity in the epithelium ($C(x,0)=C_o$).

The coupled nonlinear equations are solved numerically by finite differences using Newton–Raphson iteration to resolve the nonlinearities [93]. All 7 unknown variables are marched forward in time by a fully explicit scheme with a grid spacing of 2.5 μm. To enhance the efficiency of the computation, only half of the tear film ($0\le x\le L$) was analyzed due to symmetry.

Finally, when the fluid dynamic model changes from a Cartesian to a cylindrical coordinate system, previous derived equations are rewritten accordingly as

$$\frac{\partial h}{\partial t}=-J_e+J_w-\frac{1}{r}\frac{\partial(uhr)}{\partial r}; \tag{A19}$$

$$J_e(r,t)=\frac{1}{\tilde{\rho}_w(R_F+R_G)}\left\{\frac{P_w^{sat}(T_S)}{R_gT_S(r,t)}\exp\left(-\frac{\gamma\frac{\partial^2 h}{\partial r^2}+\Pi(h)}{\tilde{\rho}_wR_gT_S(r,t)}\right)-R_H\frac{P_w^{sat}(T_\infty)}{R_gT_\infty}\right\}; \tag{A20}$$

$$J_w(r,t)=P_c(C(r,t)-C_0); \tag{A21}$$

$$\frac{\partial(hC)}{\partial t}=-\frac{1}{r}\frac{\partial}{\partial r}\left(-Dh\frac{\partial C}{\partial r}r+uChr\right); \tag{A22}$$

$$u=\frac{h^2}{12\mu}\left(\gamma\frac{\partial^3 h}{\partial r^3}+\frac{\partial\Pi}{\partial r}\right); \tag{A23}$$

$$k_w\left(\frac{T_e-T_s(r,t)}{h}\right)+U(T_\infty-T_s(r,t))=\frac{J_e}{\rho_w}\Delta\hat{H}_v; \tag{A24}$$

and

$$H=\frac{\partial^2 h}{\partial r^2}; \tag{A25}$$

Boundary conditions are now

$$\frac{\partial h}{\partial r}=0;\quad \frac{\partial C}{\partial r}=0;\quad \frac{\partial u}{\partial r}=0\ \ and\ \ \frac{\partial H}{\partial r}=0\ \ at\ \ r=0,\pm L \tag{A26}$$

References

[1] Korb DR, Korb JM. Corneal staining prior to contact lens wearing. J Am Optom Assoc 1970;41:228–32.
[2] Norn MS. Micropunctate fluorescein vital staining of the cornea. Acta Ophthalmol 1970;48:108–18.
[3] Maurice DM. The use of fluorescein in ophthalmological research. Invest Ophthalmol Vis Sci 1967;6:464–77.
[4] Lemp MA, Hamill Jr JR. Factors affecting tear film breakup in normal eyes. Arch Ophthalmol 1973;89:103–5.
[5] Norn MS. Desiccation of the precorneal film. Acta Ophthalmol 1969;47:865–80.
[6] Liu H, Begley CG, Chalmers R, Wilson G, Srinivas SP, Wilkinson JA. Temporal progression and spatial repeatability of tear breakup. Optom Vis Sci 2006;83:723–30.
[7] Pflugfelder SC, Tseng SC, Sanabria O, Kell H, Garcia CG, Felix C, et al. Evaluation of subjective assessments and objective diagnostic tests for diagnosing tear-film disorders known to cause ocular irritation. Cornea 1998;17:38–56.
[8] Bitton E, Lovasik JV. Longitudinal analysis of precorneal tear film rupture patterns. Adv Exp Med Biol 1998;438:381–90.
[9] Mishima S. Some physiological aspects of the precorneal tear film. Arch Ophthalmol 1965;73:233–41.
[10] King-Smith E, Fink B, Hill R, Koelling K, Tiffany J. The thickness of the tear film. Curr Eye Res 2004;4:357–68.
[11] Bron AJ, Tiffany JM, Gouveia SM, Yokoi N, Voon LW. Functional aspects of the tear film lipid layer. Exp Eye Res 2004;78:347–60.
[12] Gipson IK. Distribution of mucins at the ocular surface. Exp Eye Res 2004;78:379–88.
[13] Govindarajan B, Gipson IK. Membrane-tethered mucins have multiple functions on the ocular surface. Exp Eye Res 2010;90:655–63.
[14] Cher I. Another way to think of tears: blood, sweat, and… "Dacruon". Ocul Surf 2007;5:251–4.
[15] Cher I. A new look at lubrication of the ocular surface: fluid mechanics behind the blinking eyelids. Ocul Surf 2008;6:79–86.
[16] Radke CJ, Chauhan A. Comment on: a new look at lubrication of the ocular surface–fluid mechanics behind the blinking eyelids. Ocul Surf 2008;6:152–3.
[17] Craig J. Structure and function of the preocular tear film. The tear film: structure, function and clinical examination. Butterworth-Heinemann Medical; 2002. p. 18–50.
[18] Holly FJ. Formation and rupture of the tear film. Exp Eye Res 1973;15:515–25.
[19] Creech JL. Study of the aqueous tear film and implications of contact-lens wear. [Ph.D. Thesis] University of California Berkeley; 1998 .
[20] Sharma A, Ruckenstein E. Mechanism of tear film rupture and its implications for contact lens tolerance. Am J Optom Physiol Opt 1985;62:246–53.
[21] Sharma A, Ruckenstein E. Mechanism of tear film rupture and formation of dry spots on cornea. J Colloid Interface Sci 1985;106:12–27.
[22] Lin SP, Brenner H. Tear film rupture. J Colloid Interface Sci 1982;89:226–31.
[23] Lin SP, Brenner H. Marangoni convection in a tear film. J Colloid Interface Sci 1982;85:59–65.
[24] Sharma A, Ruckenstein E. An analytical nonlinear theory of thin film rupture and its application to wetting films. J Colloid Interface Sci 1986;113:456–79.
[25] Sharma A, Ruckenstein E. The role of lipid abnormalities, aqueous and mucus deficiencies in the tear film breakup, and implications for tear substitutes and contact lens tolerance. J Colloid Interface Sci 1986;111:8–34.
[26] Israelachvili JN. Intermolecular and surface forces. 3rd ed. Academic press; 2011 189–497.
[27] Kruyt HR, Jonker GH, Overbeek JTG. Colloid science. Irreversible systems, vol. 1; 1952 .
[28] Ivanov IB. Thin liquid films: fundamentals and applications. CRC 1988; 207–75.
[29] Zhang YL, Craster RV, Matar OK. Surfactant driven flows overlying a hydrophobic epithelium: film rupture in the presence of slip. J Colloid Interface Sci 2003;264:160–75.
[30] Jones L, Dumbleton K, Hom MM, Bruce A. Soft lens extended wear and complications. Manual of contact lens prescribing and fitting. 3rd ed. Boston: Butterworth-Heinemann; 2006 393–441.
[31] Aydemir E, Breward CJW, Witelski TP. The effect of polar lipids on tear film dynamics. Bull Math Biol 2011;73:1171–201.
[32] Zhang YL, Matar OK, Craster RV. Analysis of tear film rupture: effect of non-newtonian rheology. J Colloid Interface Sci 2003;262:130–48.
[33] Zhang YL, Matar OK, Craster RV. Rupture analysis of the corneal mucus layer of the tear film. Mol Simul 2004;30:167–72.
[34] Siddique J, Braun R. Tear film dynamics with evaporation and osmolarity.Bull Am Phys Soc 2011;56 [http://meetings.aps.org/link/BAPS.2011.DFD.S30.5].
[35] Craster RV, Matar OK. Dynamics and stability of thin liquid films. Rev Mod Phys 2009;81:1131–98.
[36] Matar OK, Craster RV, Warner MRE. Surfactant transport on highly viscous surface films. J Fluid Mech 2002;466:85–111.
[37] Zubkov VS, Breward CJW, Gaffney EA. Coupling fluid and solute dynamics within the ocular surface tear film: a modelling study of black line osmolarity. Bull Math Biol 2012;74:2062–93.
[38] King-Smith PE, Fink BA, Nichols JJ, Nichols KK, Braun RJ, McFadden GB. The contribution of lipid layer movement to tear film thinning and breakup. Invest Ophthalmol Vis Sci 2009;50:2747–56.
[39] Berger RE, Corrsin S. A surface tension gradient mechanism for driving the pre-corneal tear film after a blink. J Biomech 1974;7:225–8 [IN5, 9–38].
[40] Owens H, Phillips J. Spreading of the tears after a blink: velocity and stabilization time in healthy eyes. Cornea 2001;20:484–7.
[41] Bergeron V, Fagan ME, Radke CJ. Generalized entering coefficients: a criterion for foam stability against oil in porous media. Langmuir 1993;9:1704–13.
[42] Nichols JJ, King-Smith PE, Hinel EA, Thangavelu M, Nichols KK. The use of fluorescent quenching in studying the contribution of evaporation to tear thinning. Invest Ophthalmol Vis Sci 2012;53:5426–32.
[43] King-Smith PE, Fink BA, Fogt N, Nichols KK, Hill RM, Wilson GS. The thickness of the human precorneal tear film: evidence from reflection spectra. Invest Ophthalmol Vis Sci 2000;41:3348–59.
[44] Last JA, Russell P, Nealey PF, Murphy CJ. The applications of atomic force microscopy to vision science. Invest Ophthalmol Vis Sci 2010;51:6083–94.
[45] Sharma A, Tiwari S, Khanna R, Tiffany JM. Hydrodynamics of meniscus-induced thinning of the tear film. Adv Exp Med Biol 1998;438:425–32.
[46] Tiffany JM. Measurement of wettability of the corneal epithelium. 1. Particle attachment method. Acta Ophthalmol 1990;68:175–81.
[47] Tiffany JM. Measurement of wettability of the corneal epithelium. 2. Contact-angle method. Acta Ophthalmol 1990;68:182–7.
[48] Sharma A. Relationship of thin film stability and morphology to macroscopic parameters of wetting in the apolar and polar systems. Langmuir 1993;9:861–9.
[49] Reiter G, Sharma A, Casoli A, David MO, Khanna R, Auroy P. Thin film instability induced by long-range forces. Langmuir 1999;15:2551–8.
[50] Sharma A, Khanna R, Reiter G. A thin film analog of the corneal mucus layer of the tear film: an enigmatic long range non-classical interaction in the breakup of thin polymer films. Colloids Surf B Biointerfaces 1999;14:223–35.
[51] Braun RJ. Dynamics of the tear film. Annu Rev Fluid Mech 2012:44.267–97.
[52] Iwata S, Lemp MA, Holly FJ, Dohlman CH. Evaporation rate of water from the precorneal tear film and cornea in the rabbit. Invest Ophthalmol Vis Sci 1969;8:613–9.
[53] Mishima S, Maurice DM. The oily layer of the tear film and evaporation from the corneal surface. Exp Eye Res 1961;1:39–45.
[54] Creech JL, Do LT, Fatt I, Radke CJ. In vivo tear-film thickness determination and implications for tear-film stability. Curr Eye Res 1998;17:1058–66.
[55] King-Smith PE, Nichols JJ, Nichols KK, Fink BA, Braun RJ. Contributions of evaporation and other mechanisms to tear film thinning and break-up. Optom Vis Sci 2008;85:623–30.
[56] Nichols JJ, Mitchell GL, King-Smith PE. Thinning rate of the precorneal and prelens tear films. Invest Ophthalmol Vis Sci 2005;46:2353–61.
[57] Tomlinson A, Doane MG, McFadyen A. Inputs and outputs of the lacrimal system: review of production and evaporative loss. Ocul Surf 2009;7:186–98.
[58] Mathers W. Evaporation from the ocular surface. Exp Eye Res 2004;78:389–94.
[59] King-Smith PE, Nichols JJ, Braun RJ, Nichols KK. High resolution microscopy of the lipid layer of the tear film. Ocul Surf 2011;9:197–211.
[60] Cerretani CF, Ho NH, Radke CJ. Water-evaporation reduction by duplex films: application to the human tear film. Adv Colloid Interface Sci 2013. http://dx.doi.org/10.1016/jcis201303007.
[61] Kimball SH, King-Smith PE, Nichols JJ. Evidence for the major contribution of evaporation to tear film thinning between blinks. Invest Ophthalmol Vis Sci 2010;51:6294–7.
[62] King-Smith PE, Hinel EA, Nichols JJ. Application of a novel interferometric method to investigate the relation between lipid layer thickness and tear film thinning. Invest Ophthalmol Vis Sci 2010;51:2418–23.
[63] Cerretani C, Takatori S, Radke CJ. Stability of liquid rivulets on liquid substrate.Bull Am Phys Soc 2011;56 [http://meetings.aps.org/Meeting/DFD11/Event/155917].
[64] Braun RJ, King-Smith PE, Nichols JJ, Rawamoorthy P. On computational models of tear film and osmolarity dynamics. The 6th International Conference on the Tear Film & Ocular Surfaces; 2010 [Florence, Italy].
[65] Liu H, Begley C, Chen M, Bradley A, Bonanno J, McNamara NA, et al. A link between tear instability and hyperosmolarity in dry eye. Invest Ophthalmol Vis Sci 2009;50:3671–9.
[66] McDonald JE, Brubaker S. Meniscus-induced thinning of tear films. Am J Ophthalmol 1971;72:139–46.
[67] Miller KL, Polse KA, Radke CJ. Black-line formation and the "perched" human tear film. Curr Eye Res 2002;25:155–62.
[68] Braun RJ, Usha R, McFadden GB, Driscoll TA, Cook LP, King-Smith PE. Thin film dynamics on a prolate spheroid with application to the cornea. J Eng Math 2012;73:121–38.
[69] Leung BK, Bonanno JA, Radke CJ. Oxygen-deficient metabolism and corneal edema. Prog Retin Eye Res 2011;30:471–92.
[70] Fatt I, Weissman BA. Physiology of the eye: an introduction to the vegetative functions. 2nd ed. Boston, MA: Butterworth-Heinemann; 1992; 85–204.
[71] Winter KN, Anderson DM, Braun RJ. A model for wetting and evaporation of a post-blink precorneal tear film. Math Med Biol 2010;27:211–25.
[72] Bird RB, Stewart WE, Lightfoot EN. Transport phenomena. revised 2nd ed. Wiley; 2006 40–141.
[73] Deen WM. Analysis of transport phenomena. Oxford University Press; 1998 270–82.
[74] Berg JC. Introduction to interfaces and colloids. World Scientific Publishing Company Inc.; 2009 84–6.
[75] Hisatake K, Fukuda M, Kimura J, Maeda M, Fukuda Y. Experimental and theoretical study of evaporation of water in a vessel. J Appl Phys 1995;77:6664–74.
[76] Baldwin PEJ, Maynard AD. A survey of wind speeds in indoor workplaces. Ann Occup Hyg 1998;42:303–13.
[77] Li L, Braun RJ. A model for the human tear film with heating from within the eye. Phys Fluids 2012;24:062103.
[78] Craig JP, Tomlinson A. Importance of the lipid layer in human tear film stability and evaporation. Optom Vis Sci 1997;74:8–13.
[79] Fornasiero F, Prausnitz JM, Radke CJ. Post-lens tear-film depletion due to evaporative dehydration of a soft contact lens. J Membr Sci 2006;275:229–43.
[80] Chin DT, Tsang CH. Mass transfer to an impinging jet electrode. J Electrochem Soc 1978;125:1461–70.

[81] McCulley JP, Aronowicz JD, Uchiyama E, Shine WE, Butovich IA. Correlations in a change in aqueous tear evaporation with a change in relative humidity and the impact. Am J Ophthalmol 2006;141:758–60.

[82] Uchiyama E, Aronowicz JD, Butovich IA, McCulley JP. Increased evaporative rates in laboratory testing conditions simulating airplane cabin relative humidity: an important factor for dry eye syndrome. Eye Contact Lens 2007;33:174–6.

[83] Nagyova B, Tiffany JM. Components responsible for the surface tension of human tears. Curr Eye Res 1999;19:4–11.

[84] Miller D. Measurement of the surface tension of tears. Arch Ophthalmol 1969;82: 368–71.

[85] Tiffany JM, Winter N, Bliss G. Tear film stability and tear surface tension. Curr Eye Res 1989;8:507–15.

[86] Tiffany JM. The lipid secretion of the meibomian glands. Adv Lipid Res 1987;22:1–62.

[87] Ajaev VS. Evolution of dry patches in evaporating liquid films. Phys Rev E 2005;72:031605.

[88] Ajaev VS. Spreading of thin volatile liquid droplets on uniformly heated surfaces. J Fluid Mech 2005;528:279–96.

[89] Rosenfeld L, Cerretani C, Leiske DL, Toney MF, Radke CJ, Fuller GG. Structural and rheological properties of meibomian lipid. Invest Ophthalmol Vis Sci 2013;54: 2720–32.

[90] Yeh EK, Newman J, Radke CJ. Equilibrium configurations of liquid droplets on solid surfaces under the influence of thin-film forces part I. Thermodynamics. Colloids Surf A Physicochem Eng Aspects 1999;156:137–44.

[91] Levin MH, Verkman AS. Aquaporin-dependent water permeation at the mouse ocular surface: in vivo microfluorimetric measurements in cornea and conjunctiva. Invest Ophthalmol Vis Sci 2004;45:4423–32.

[92] Welty JR. Fundamentals of momentum, heat, and mass transfer. 4th ed. John Wiley & Sons Inc.; 2001 725–40.

[93] Newman JS, Thomas-Alyea KE. Electrochemical systems. 3rd ed. Wiley-Interscience; 2004 611–34.

[94] Sandler SI. Chemical, biochemical, and engineering thermodynamics. Hoboken, New Jersey: John Wiley& Sons Inc.; 2006 A1–A14.

[95] Wong H, Fatt I, Radke CJ. Deposition and thinning of the human tear film. J Colloid Interface Sci 1996;184:44–51.